Hartmann flow
in annular channels. Part 2. Numerical solutions for
low to moderate Hartmann numbers

By C. J. APELT

University of Queensland, Brisbane, Australia

Flow of a conducting fluid along the annular channel between two non-conducting circular cylinders is examined by a numerical method for concentric and eccentric cases. Solutions have been obtained for Hartmann numbers ranging from 0·1 to 40 and, for some of these, details of velocity distribution and of induced current are given. The results obtained enable the development of the patterns of velocity and of current flow to be traced as the Hartmann number increases. The details of the development of the current flow patterns for eccentric cylinders are particularly interesting and are discussed in detail. At the higher values of Hartmann number studied the solutions are in excellent agreement with the results of Todd's (1967) high Hartmann number analysis and it is possible to determine at what value of Hartmann number Todd's analysis becomes applicable within a specified accuracy. The effect of eccentricity of the cylinders on the flow rate at a fixed pressure gradient is shown to diminish rapidly with increasing Hartmann number. The net flow of current around the annulus, which occurs when the cylinders are eccentric, has a maximum value for each case studied at a Hartmann number of 3, approximately.

1. Introduction

The pressure-driven flow of a conducting fluid along the annular channel between two non-conducting circular cylinders in the presence of a transverse magnetic field has been analysed by Todd (1967) for the case of large Hartmann number. Todd's analysis indicated the existence of essentially four régimes in the flow; Hartmann layers on the boundaries of the cylinders, 'obscure regions' in the neighbourhood of the points on the boundaries where the applied field is tangential to the boundary, core regions in which the velocity is uniform and transition regions or 'wakes' dividing the core regions in the neighbourhood of the planes parallel to the applied field and tangential to the inner cylinder.

From its nature, Todd's analysis is valid only for large Hartmann number and it is of considerable interest to determine how the velocity distribution and the current flow pattern at small Hartmann number develop into their asymptotic forms and also to determine what value of the Hartmann number must be attained for the large Hartmann number analysis to be applicable. Uflyand (1961) pointed out that, when the cylinders are concentric, the exact solution

14

may be obtained in the form of infinite series and it would be possible to extract from this solution, numerically, the kind of information mentioned above. However, the infinite series involve modified Bessel functions and the computational effort required to produce detailed information from the solution is large even for small values of Hartmann number. For larger values of Hartmann number the series becomes very inconvenient for computation, as Gold (1962) found in the simpler case of flow through a circular pipe.

In view of the above difficulties it was considered that it would be more efficient even for the case of concentric cylinders, to produce the information required by direct numerical solution of the governing equations rather than by numerical evaluation from the series solution. Further, the direct numerical solution could be applied with relatively small increase in difficulty to the case of eccentric cylinders for which no exact solution is available. This paper describes the method developed for numerical solution of the governing equations and presents some detailed results of solutions for concentric and eccentric cylinders for values of Hartmann number up to 40. The solutions at the higher values of Hartmann number are in close agreement with the results from Todd's analysis for large Hartmann number.

2. The governing equations and boundary conditions

The governing equations for unidirectional flow of a viscous incompressible conducting fluid perpendicular to a uniform applied magnetic field (Shercliff 1953) are

$$\lambda \nabla^2 B_z + B_0 \frac{\partial V_z}{\partial x} = 0, \tag{1}$$

$$\eta \nabla^2 V_z + \frac{B_0}{\mu} \frac{\partial B_z}{\partial x} = -P, \tag{2}$$

$$\frac{\partial}{\partial x}, \quad \frac{\partial}{\partial y}, \quad \left(p + \frac{B_z^2}{2\mu} \right) = 0. \tag{3}$$

The notation is the same as that of Todd (1967); p, η and λ are the fluid pressure, dynamic viscosity and magnetic diffusivity respectively, μ the (absolute) magnetic permeability, $-P = \partial p/\partial z = $ constant, and $B = (B_0, 0, B_z)$, where B_0 is the applied magnetic field. The only component of the fluid velocity is V_z. Here B_z is the stream function for current, i.e. current flows along the curves $B_z = $ constant.

The problem considered is the case of pressure-driven flow through the annular channel between two insulating circular cylinders of radii a, b $(b > a)$. The centres of the cylinders are eccentric by an amount γ $(0 \leqslant \gamma < b-a)$ (figure 1). In all cases studied, the relative displacement of the cylinders was parallel to the direction of $\mathbf{B}_0$.†

---

† Todd (1967) inferred that, for large Hartmann number, the only effect of relative displacement of the cylinders in the direction perpendicular to $\mathbf{B}_0$ is to shift the patterns of V_z and B_z in that direction. In view of this result it was decided not to consider cases with such displacement in order to obtain as much detail as possible about the effects of displacements in the $\mathbf{B}_0$ direction, within the relatively restricted budget of computer time available.

The velocity V_z must vanish at the cylinder boundaries. B_z may be assumed to vanish on the outer boundary and, on the inner boundary, B_z must take a constant value, say B_{z_i}. Todd (1967) has pointed out that $B_{z_i} = \mu I$, where I is the net amount of current flowing around the annulus per unit length and he showed that B_{z_i} is zero for all Hartmann numbers when $\gamma = 0$, whether or not the cylinders are displaced in the direction perpendicular to $\mathbf{B_0}$. He also showed that, for Hartmann numbers $\gg 1$, $I \neq 0$ if $\gamma \neq 0$. While it has not been proved that $I \neq 0$ if $\gamma \neq 0$ for all Hartmann numbers, all the numerical solutions obtained do give this result.
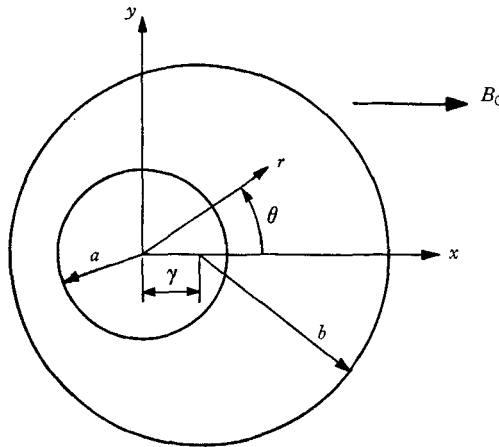

FIGURE 1. Notation.

Since the conditions of the problem are invariant with time,

$$\text{curl } \mathbf{E} = -\partial \mathbf{B}/\partial t = 0,$$

where $\mathbf{E}$ is the electric field strength and, hence, for any closed circuit

$$\oint \mathbf{E} . d\mathbf{s} = 0. \tag{4}$$

If the circuit is the boundary of the inner cylinder, this condition becomes (Hasimoto 1960)

$$\int_0^{2\pi} \left(\frac{\partial B_z}{\partial r} \right)_{r=a^+} d\theta = 0. \tag{5}$$

For the purposes of numerical solution it is convenient to reduce the equations and boundary conditions to dimensionless form. There are several possible ways of doing this, but the most suitable set of dimensionless variables for the problems considered here are $x' = x/a$, $y' = y/a$, $V = V_z(B_0 \sigma^{\frac{1}{2}} \eta^{\frac{1}{2}}/aP)$, $B = B_z(B_0/\mu aP)$, in which σ is the electrical conductivity of the fluid. Equations (1) and (2) become,

$$M^{-1} \nabla^2 B + \frac{\partial V}{\partial x'} = 0, \tag{6}$$

$$M^{-1} \nabla^2 V + \frac{\partial B}{\partial x'} = -1, \tag{7}$$

where $\qquad\qquad \nabla^2 \equiv \dfrac{\partial^2}{\partial x'^2} + \dfrac{\partial^2}{\partial y'^2}$ and $M = B_0(\sigma/\eta)^{\frac{1}{2}}a,$

the Hartmann number based on the radius of the inner cylinder. If the radius of the inner cylinder is chosen to be unity, the primes can be dropped from the space variables without danger of confusion and this will be done in the remainder of the paper.

Introduction of the auxiliary variables,

$$m = V + (x+B), \quad n = V - (x+B), \qquad\qquad (8), (9)$$

enables (6), (7) to be decoupled, giving:

$$\nabla^2 m + M\,(\partial m/\partial x) = 0, \qquad\qquad (10)$$

$$\nabla^2 n - M\,(\partial n/\partial x) = 0. \qquad\qquad (11)$$

3. Numerical solutions

Concentric cylinders

For the case of concentric cylinders the numerical solution of (10) and (11) can proceed in a straightforward manner. The boundary conditions on both inner and outer cylinder are $m = x$, $n = -x$ and (10) and (11) are solved separately. The chief difficulty arises from the boundary geometry and the manner of dealing with this is described in a later section.

Eccentric cylinders

When the cylinders are eccentric, the value of B on the inner cylinder is unknown, and must be found as part of the solution. The correct value of B is that which ensures that the solution satisfies the integral condition (4). Usually such a problem poses great difficulties for numerical solution, but, in this case, the linearity of the equations simplifies the problem. Solution is achieved by breaking the problem into two parts. Firstly, the equations (6), (7) are solved with boundary conditions $B = 0$, $V = 0$ on both inner and outer cylinder. The equations are solved in the decoupled form (10) and (11) and the problem is essentially the same as for the concentric case. Secondly, the equation (6) coupled with the equation,

$$M^{-1}\nabla^2 V + (\partial B/\partial x) = 0, \qquad\qquad (12)$$

is solved with boundary conditions $B = 0$, $V = 0$ on the outer cylinder and $B = 1$, $V = 0$ on the inner cylinder. Equations (6) and (12) are decoupled by use of the auxiliary variables

$$m_1 = V + B, \quad n_1 = V - B, \qquad\qquad (13), (14)$$

giving a pair of equations identical in form to (10), (11) with m_1 and n_1 replacing m and n respectively. For each of these two cases the integral on the left of (4) is evaluated for a given circuit. If the value of the integral is respectively I_1 and I_2, the required solution which satisfies the boundary conditions and the integral condition (4) is given by the linear combination of the solutions of the first and second cases in the proportions $1:k$ such that

$$I_1 + kI_2 = 0. \qquad\qquad (15)$$

The value of k given by (15) is the desired constant value of B on the inner cylinder.

It is of interest to note that $I_2 \neq 0$. For if it is assumed that $I_2 = 0$, the result obtained by Todd (1967) in his consideration of the pair of equations (6) and (12) gives $\nabla B_z = 0$, whence $B_z = 0$ on the inner cylinder. But this is in contradiction with the specified boundary condition $B_z = 1$ on the inner cylinder and it follows that $I_2 \neq 0$.†

Dealing with the boundary geometry

In the preceding sections it has been shown that the numerical solution of both the concentric and the eccentric case can be reduced to the problem of solution of equations of the form (10) and (11) with values of the dependent variables specified on the cylinder boundaries. Equations (10) and (11) are of elliptic type and the only significant difficulty in their numerical solution by finite difference techniques arises from the curved boundary geometry which leads to irregular mesh lengths if the solution is calculated in the xy-plane. This difficulty was overcome by use of the method of 'symmetromorphic figures' developed by Thom & Apelt (1961). The solution domain is mapped conformally on an auxiliary plane, the transformation being so chosen that the solution domain in the xy-plane maps on to the interior of a rectangle in the auxiliary plane and, equally important, it is so arranged that the rectangle in the auxiliary plane is divided into an integral number of equal mesh lengths in both dimensions.

If the transformation is given by the function $w = f(z)$ where $z = x + iy$ and $w = \phi + i\psi$, (10), (11) are transformed into

$$\nabla^2_{\phi\psi} m + \frac{M}{Q}\left(\cos\alpha\,\frac{\partial m}{\partial\phi} + \sin\alpha\,\frac{\partial m}{\partial\psi}\right) = 0, \tag{16}$$

$$\nabla^2_{\phi\psi} n - \frac{M}{Q}\left(\cos\alpha\,\frac{\partial n}{\partial\phi} + \sin\alpha\,\frac{\partial n}{\partial\psi}\right) = 0, \tag{17}$$

where $\qquad Q = |\,dw/dz\,| \quad$ and $\quad \alpha = \arg\,(dw/dz).$

The transformations used were

$$w = -\Gamma\ln z \tag{18}$$

for the concentric case and $\qquad w = -\Gamma\ln\dfrac{z-\kappa}{z+\kappa} \tag{19}$

for the eccentric case. In each case the appropriate function maps the annular region between the cylinders, with a cut placed along the negative x-axis, on to a rectangular region in the w-plane. If the relative magnitudes of the dimensions a, b and γ in the z-plane were specified in advance, it would in general be possible to subdivide each dimension of the rectangular region in the w-plane into an integral number of equal mesh lengths only by using different mesh lengths for the two directions. However, it is possible to achieve a solution domain in the w-plane which can be subdivided integrally by a square mesh by specifying the proportions of the rectangle in the w-plane and accepting the proportions pro-

† The author is indebted to a reviewer for drawing attention to this proof.

duced by the transformation in the z-plane. For the concentric case the solution domain in the w-plane was arranged to be a rectangle with sides in the ratio 8 to 1. This gave cylinders in the z-plane whose radii are in the ratio 2·193 to 1. For the eccentric case the values of the parameters in the transformation, (19), were selected to give, to an acceptable approximation, the same ratio of radii as for the concentric case for a number of different eccentricities, while still mapping a rectangle in the w-plane which could be subdivided integrally by a square mesh. The proportions of the several cases studied are given in table 1.

γ/a	b/a	Ratio of sides of rectangle
0	2·193	8
0·0752	2·196	8
0·1209	2·201	8
0·3867	2·199	$8\frac{2}{5}$
0·5543	2·191	9
0·7744	2·186	$10\frac{1}{2}$
1·0000	2·186	$14\frac{2}{3}$

TABLE 1. Proportions of channels for which numerical solutions have been obtained.

Solution of the difference equations

The equations (16), (17) were converted into finite-difference relations, and the set of simultaneous algebraic equations produced by writing the difference equation at each interior mesh point of the solution domain was solved by an iterative procedure which was proposed by Russell (1962) as being the best method for solving finite-difference equations of the type involved. Russell designated the method 'successive optimum displacement by points'. At the rth iteration the value of the function m at each mesh point is obtained from

$$m_{j,k}^{(r)} = (1 - \omega_{j,k}) m_{j,k}^{(r-1)} + \tfrac{1}{4}\omega_{j,k}[(1 - A_{j,k}) m_{j-1,k}^{(r)} + (1 + A_{j,k}) m_{j+1,k}^{(r-1)}$$
$$+ (1 - B_{j,k}) m_{j,k-1}^{(r)} + (1 + B_{j,k}) m_{j,k+1}^{(r-1)}], \qquad (20)$$

$$\omega_{j,k} = 2[1 + \{\tfrac{1}{2}[A_{j,k}^2 + B_{j,k}^2 + \pi^2(u^{-2} + v^{-2})]\}^{\frac{1}{2}}]^{-1}, \qquad (21)$$

in which $A_{j,k} = Mh\cos\alpha_{j,k}/2Q_{j,k}$; $B_{j,k} = Mh\sin\alpha_{j,k}/2Q_{j,k}$; h is the mesh length, subscripts j, k are the mesh co-ordinates corresponding to the ϕ and ψ dimensions respectively, and u and v are the number of intervals of the mesh along the two sides of the rectangular domain in which the solution is being calculated. The equation for the function n is similar to (20) except that the signs preceding the coefficients A and B are everywhere reversed. The iterative process defined by (20), (21) differs from that designated by Young (1954) as successive over-relaxation in that ω is here a function of ϕ and ψ and may be less than 1, depending on the values of A and B. In the special case, $A = B = 0$ (16), (17) become Laplace's equation and the iterative process of (20), (21) becomes identical to that of successive over-relaxation (SOR). The iterative process proved to be very efficient over a wide range of values of A and B.

Control of accuracy of solution

The iterations were stopped when residuals in the difference equations corresponding to (16) and (17) were everywhere less than 10^{-6} times the order of magnitude of m and n in the solution. In a preliminary study it was found that, when each cycle of iteration progressed in the same direction from one end of the solution domain to the other, a significant bias was introduced into the solution. This bias was eliminated when the sequence of iteration was so arranged that, for each cycle, the iteration proceeded simultaneously from opposite ends of the solution domain in opposite direction.

A number of checks of the accuracy of the values of V and B as produced from the solutions for m and n was conducted, as follows: (i) The values of V and B were substituted into the finite difference equivalents of (6), (7) for each mesh point and the residuals evaluated. The maximum and the overall average values of the residuals were determined. (ii) The overall force balance between the pressure gradient forces, electromagnetic forces and viscous shear forces for the whole flow cross-section was checked. (iii) For the case of eccentric cylinders, the integral on the left of (4) was evaluated for two different circuits enclosing the inner cylinder, one being a circle which was located approximately half-way between the inner and outer cylinders and the other being the inner cylinder itself. (iv) The solution at each value of Hartmann number was obtained for several different intervals of subdivision of the mesh. For the concentric case, the solution was obtained for three different mesh lengths and for the eccentric case two mesh lengths were used. It was intended initially that a process such as the 'deferred approach to the limit' due to Richardson & Gaunt (1926) would be employed to extrapolate to the case of vanishingly small mesh length but experience with the concentric case indicated that this would be of dubious value in the present context. However, the solutions at the different mesh lengths did permit an estimate to be made of the accuracy of the integral results obtained from them.

Poiseuille flow

For the limiting case of $M = 0$ which corresponds to Poiseuille flow, the problem reduces to the solution of the equation

$$\eta \nabla^2 V_z = -P. \tag{22}$$

For the eccentric case this equation was solved numerically. The occurrence of irregular mesh lengths was avoided by use of the method of 'symmetromorphic figures' in exactly the same manner as described for the Hartmann flow solutions. Otherwise, the numerical procedure employed standard methods of SOR and does not warrant detailed discussion here.

4. Results obtained

Numerical solutions were obtained for values of Hartmann number 0, 0·1, 1, 5, 10, 20 and 40 for the concentric case and for the five different eccentricities given in table 1. At the finest subdivision of the mesh the gap between the inner and outer cylinder was divided into thirty-two intervals in the concentric case and between sixteen and twenty intervals in the eccentric cases. At $M = 40$ the thickness of the boundary layers at their narrowest part had shrunk to a dimension comparable to these mesh lengths, and accurate solutions for $M > 40$ could be obtained only by using finer subdivision of the mesh in the region of the
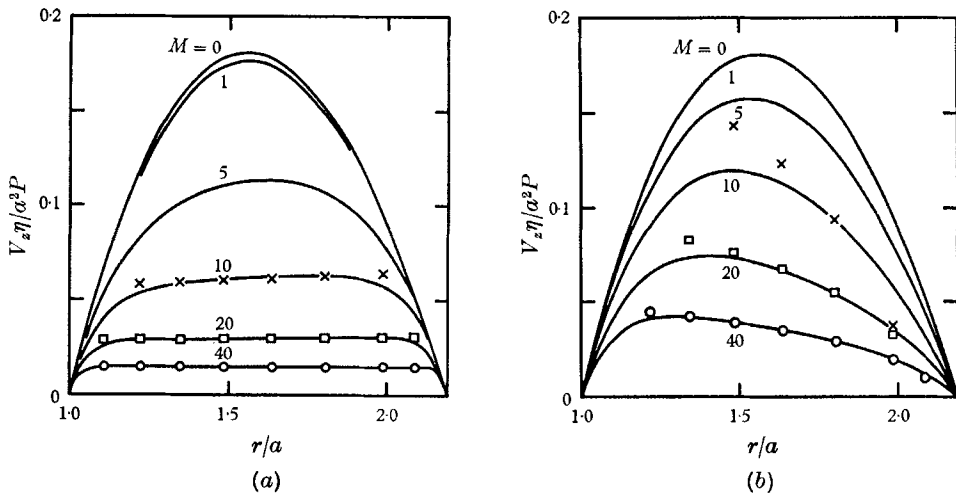
FIGURE 2. (a) Velocity profiles for concentric cylinders at $\theta = 0°$. ——, numerical solution; $\times$, $\square$, $\bigcirc$, values calculated from large Hartmann number analysis for $M = 10$, 20 and 40 respectively. (b) Velocity profiles for concentric cylinders at $\theta = 90°$. ——, numerical solution; $\times$, $\square$, $\bigcirc$, values calculated from large Hartmann number analysis for $M = 10$, 20 and 40 respectively.

boundary layers. However, at $M = 40$ the solutions already displayed all of the features of the high Hartmann number solution obtained by Todd (1967) and it is considered that there is little to be gained from obtaining numerical solutions for values of $M > 40$.

4.1. Concentric cylinders

A selection of the results obtained is presented in the accompanying figures. Velocity profiles along radial sections at $\theta = 0°$ and $90°$ for the concentric case are shown in figures 2 (a) and (b) respectively. The velocity, V_z, is plotted as the dimensionless form $V_z\eta/a^2P$. The axial symmetry of the Poiseuille flow ($M = 0$) is destroyed by the application of the transverse magnetic field. From the velocity profiles of figures 2 it can be seen that the distortion of the Poiseuille flow is quite small for $M < 1$, but that as M is increased beyond 1 the velocity distribution is completely changed by the effects of the electro-magnetic forces. At $M = 20$, V_z is almost constant across most of the section at $\theta = 0°$ and Hart-

mann boundary layers have developed near each cylinder wall. As M is increased to 40 there is relatively little change in the shape of the velocity profiles except that the boundary layers have become thinner. For a specific channel with a fixed pressure gradient driving the flow the velocity profiles show how V_z is reduced in magnitude as the applied magnetic field B_0 is increased in strength. At $M = 40$ the maximum velocity at $\theta = 0°$ is only 0·084 of the maximum value for the Poiseuille flow. Some values of V_z have been calculated from Todd's solutions for the core flows for $M \gg 1$ and are plotted in figures 2(a) and (b). At $\theta = 0°$, figure 2(a), the velocity distribution given by the numerical solution has ap-
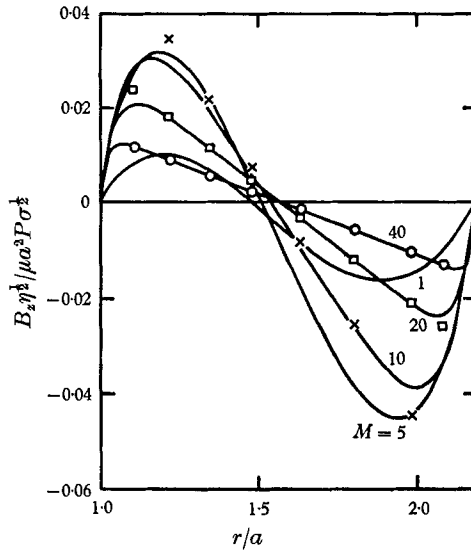
FIGURE 3. Distribution of induced magnetic field for concentric cylinders at $\theta = 0°$. ———, numerical solution; ×, □, ○, values calculated from large Hartmann number analysis for $M = 10$, 20 and 40 respectively.

proached closely to the asymptotic result over approximately half of the flow passage at $M = 10$, and at $M = 20$ and 40 the two solutions are virtually indistinguishable except in the region of the boundary layers, to which the asymptotic core solution does not apply. The comparison between the two solutions at $\theta = 90°$, figure 2(b), shows that close agreement is not reached until $M \sim 20$, and that at $M = 40$, while the two solutions are indistinguishable over a large proportion of the flow passage, the regions near the boundaries to which the asymptotic core solution does not apply are more extensive than for the section at $\theta = 0°$. This result is consistent with Todd's solution for $M \gg 1$. He found that 'obscure' regions exist in the region $|\frac{1}{2}\pi - |\theta|| \sim M^{-\frac{1}{2}}$ near each cylinder, the thickness of the obscure regions being $O(aM^{-\frac{2}{3}})$ and $O(bM^{-\frac{2}{3}})$ at the inner and outer cylinder respectively (see also Waechter 1968). In these regions, neither the boundary layer solution nor the core solution applies.

The distribution of induced magnetic field along the radial section at $\theta = 0°$ for the concentric case is shown in figure 3. B_z is plotted as the dimensionless form $B_z \eta^{\frac{1}{2}}/\mu a^2 P \sigma^{\frac{1}{2}}$. The profiles show that, as the Hartmann number increases,

regions of linear distribution of B_z develop in the centre of the flow and become more extensive, ultimately occupying all the cross section except for narrow regions near each boundary, corresponding to the boundary layers referred to above. For a specific channel with a fixed pressure gradient the profiles of figure 3 show that the maximum absolute value of B_z first increases with increasing value
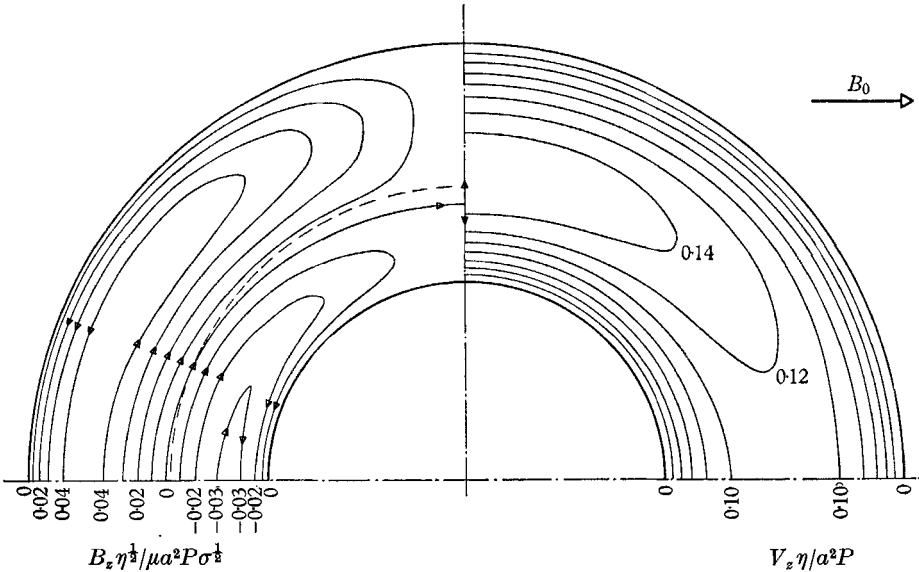

FIGURE 4. Distributions of velocity and of induced magnetic field for concentric cylinders at $M = 5$. — — — —, current line $B_z = 0$ at $M = 1$.
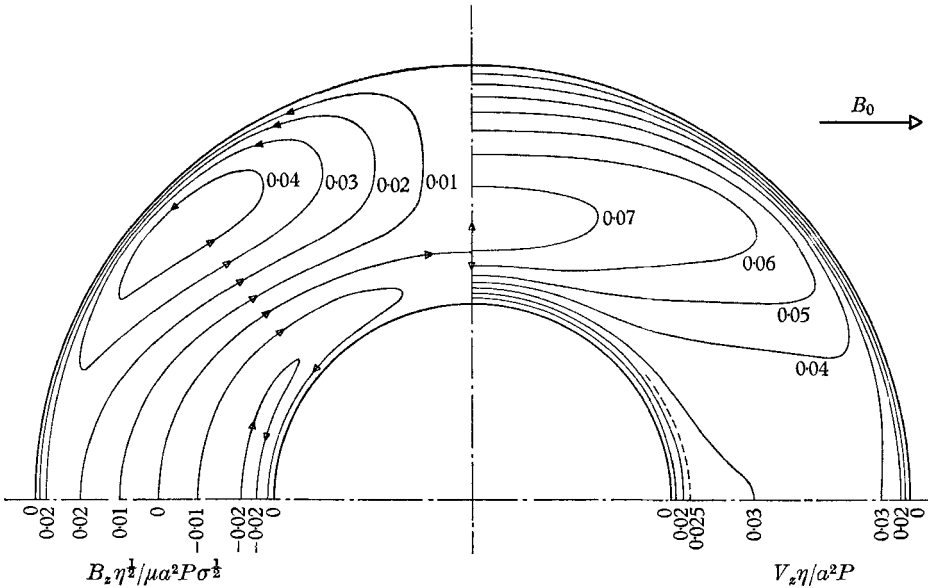
FIGURE 5. Distribution of velocity and of induced magnetic field for concentric cylinders at $M = 20$.

of B_0 but then decreases as B_0 is further increased. Comparison is made between the values of B_z obtained from the numerical solutions and from Todd's core solution for $M \gg 1$ at $\theta = 0°$ in figure 3. The distributions of B_z given by the two solutions are virtually indistinguishable for $M \geqslant 20$ except in the region of the boundary layers.

The distributions of V_z and B_z over the flow section of the concentric case are shown for $M = 5$ in figure 4 and for $M = 20$ in figure 5. Since V_z is even in x and y and B_z is odd in x and even in y, only one quarter of each distribution needs to
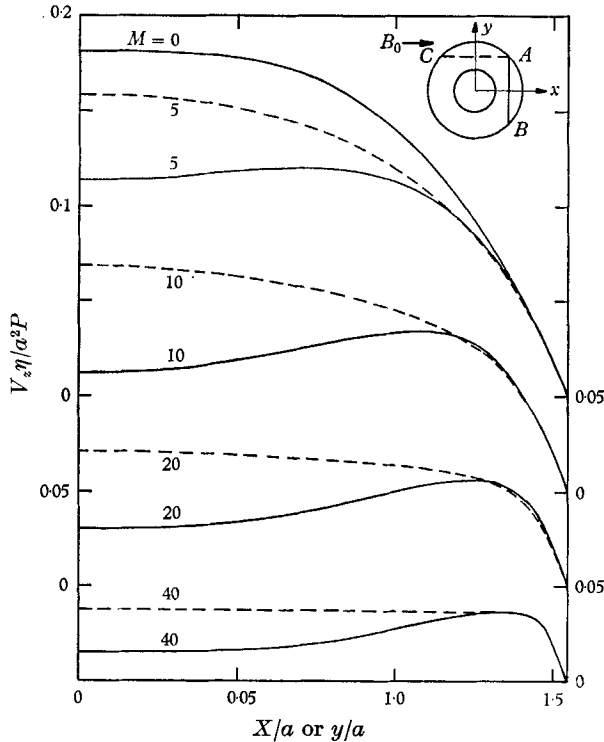
FIGURE 6. Velocity profiles for concentric cylinders showing development of core regions and of shear layers. ———, profile along AB, — — — —, profile along AC. Profiles for different values of M are displaced vertically for greater clarity. The profiles are symmetrical about the x or y axis and only half of each is shown.

be plotted. In these figures contours of constant B_z also represent current lines, as noted previously. At $M = 5$ (figure 4) the velocity contours show the beginnings of two regions of nearly uniform velocity corresponding to $|y| < a$ and $|y| > a$. Following Todd (1967) these regions will be described as the inner core and the outer core respectively. At $M = 20$ (figure 5) the velocity contours show well developed core regions and the velocity increases from its low value in the inner core to the much larger value in the outer core across a region of relatively large transverse velocity gradient in the vicinity of $|y| = a$. This is the shear layer or 'wake' described by Todd. It is still relatively diffuse at $M = 20$† but becomes

† This is to be expected since Todd showed that the wake thickness is small compared to a only for $M^{\frac{1}{2}} \gg 1$.

narrower as M increases further. The Hartmann boundary layers near each cylinder wall are well developed at $M = 20$. The apparently anomalous shape of the velocity contour with value 0·03 results from the fact that it emerges from the boundary-layer region into the very nearly uniform core region near $\theta = 0°$. The contour with value 0·025 is approximately at the edge of the boundary layer in this region. The maximum velocity gradient occurs near $\theta = \pm 45°$ and $\pm 135°$ in the boundary layer on the outer cylinder wall. The development of the core regions and of the shear layers are further illustrated in figure 6, where velocity profiles are plotted along sections across the core regions and the wake. The profiles across the outer core show that at $M = 40$, V_z is nearly independent of x (the solution for $M \gg 1$ gives V_z independent of x in the outer core.)

The pattern of current lines at $M = 5$, figure 4, is only slightly different from that at lower values of M. (The current line corresponding to $B_z = 0$ at $M = 1$, which is essentially concentric with the cylinders has been included in figure 4 for comparison.) The chief points of interest in the pattern at $M = 5$ are the slight local maximum in $|B_z|$ near $\theta = \pm 45°$ and $\pm 135°$ and the current flow stagnation points at $\theta = \pm 90°$, where the current line, $B_z = 0$, branches at saddle points. However, by $M = 20$, the pattern of current lines, figure 5, is in essential agreement with that obtained by Todd for $M \gg 1$ except for the presence of the pronounced maximum in $|B_z|$ and the associated local maximum in boundary-layer current in the vicinity of $\theta = \pm 45°$, $\pm 135°$ near the outer cylinder boundary. Although not adverted to by Todd, this feature is implicit in his solution. The core velocity is proportional to the boundary layer current, as pointed out by Shercliff (1956), and, since the outer core velocity is approximately twice that in the inner core, the associated difference in the boundary-layer currents requires the existence of the pattern of current lines appearing in the upper part of figure 5. It is obvious from the foregoing that this feature must persist for $M \gg 1$, undergoing only some modification in shape as the boundary layers become thinner. The presence of the maxima in $|B_z|$ at $\theta = \pm 45°$, $\pm 135°$ causes the formation of saddle points in the distribution of B_z at $\theta = 0°$, $180°$ and stagnation points in the current flow there.

4.2. *Eccentric cylinders*

Some detailed results for one geometry of eccentric cylinders ($\gamma/a = 0·5543$) are presented in figures 7–11. The solutions for other eccentricities are generally similar to those shown. The velocity distribution for the Poiseuille case, figure 7, shows pronounced asymmetry, the maximum velocity where the gap between cylinders is greatest being approximately five times as great as that where the gap is narrowest. The effect of the applied magnetic field is to make the velocity distribution progressively more and more like that for the concentric case as M increases, until at $M = 20$, figure 8, the velocity distribution has become quite similar to that for concentric cylinders at the same value of M (figure 5), with the development of Hartmann boundary layers and of inner and outer core flows separated by shear layers. Todd (1967) found that the velocity distribution for eccentric cylinders is the same as for the concentric case for $M \gg 1$.

The development of the current flow pattern as M increases, which is shown

in figures 9, 10, 11 and 12(b) is very interesting. For all values of M, some current flows right round the inner cylinder. In the narrowest gap between the cylinders, at low values of M all the current flows in the direction of negative y, opposite to the direction of the induced e.m.f., as shown in figures 9 and 10 for $M = 1$ and 5 respectively. However, as M increases and the core flows and Hartmann boundary layers develop, current flows in the direction of positive y in the core region of the narrow gap, returning through the boundary layers to form closed current loops. The details of the development of the current flow pattern, as M increases from low values, varies with the eccentricity of the cylinders. The value of M at which current begins to flow in the positive y direction in the central region of the narrow gap increases with γ/a. For $\gamma/a = 0.0752$ and 0.1209, this situation has
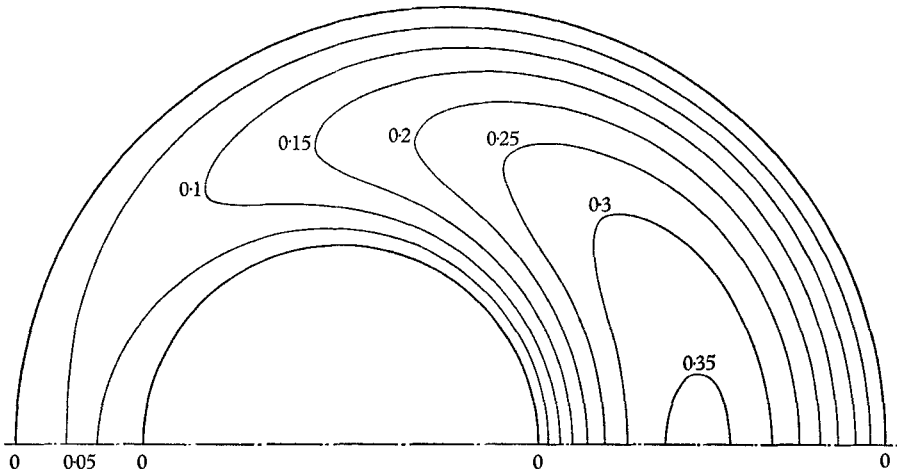

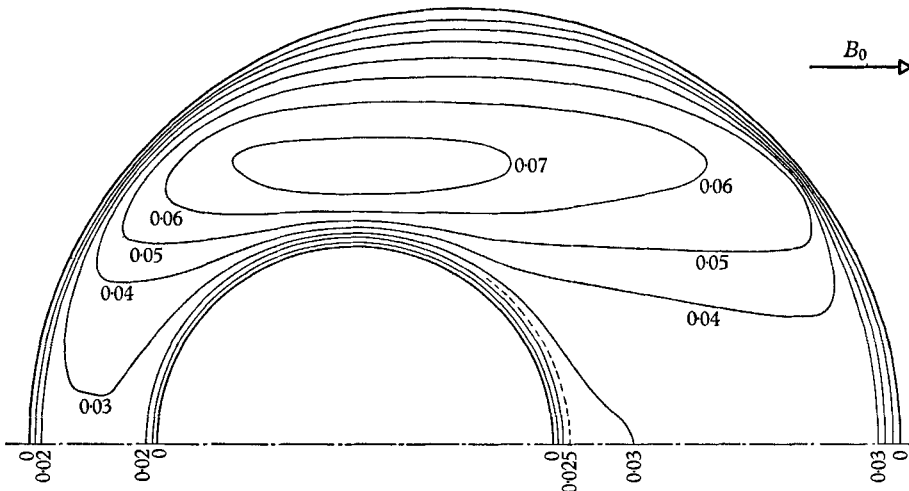FIGURE 7. Distribution for eccentric cylinders; Poiseuille case. Contours of $V_z\eta/a^2P$ at intervals of 0.05.

FIGURE 8. Distribution of velocity for eccentric cylinders at $M = 20$. Contours of $V_z\eta/a^2P$ at intervals of 0.01.

developed already at the smallest value of M considered (0·1); for $\gamma/a = 0·3867$, it develops between $1 < M < 5$; for $\gamma/a = 0·5543$, between $5 < M < 10$; for $\gamma/a = 0·7744$, between $10 < M < 20$; and for $\gamma/a = 1·0$, it has just begun to develop at $M = 40$. The greater the eccentricity, the greater is the difference between the velocities in the wide and narrow gap for Poiseuille flow and, hence, the greater is the difference between the induced e.m.f. in these regions at low values of M. Initially, current flows in the narrow gap opposite to the direction of the local induced e.m.f., but the consequent differences in electromagnetic forces progressively reduces the differences in velocity in the two regions as M is increased and, in fact, initially the velocity in the narrow gap increases while the
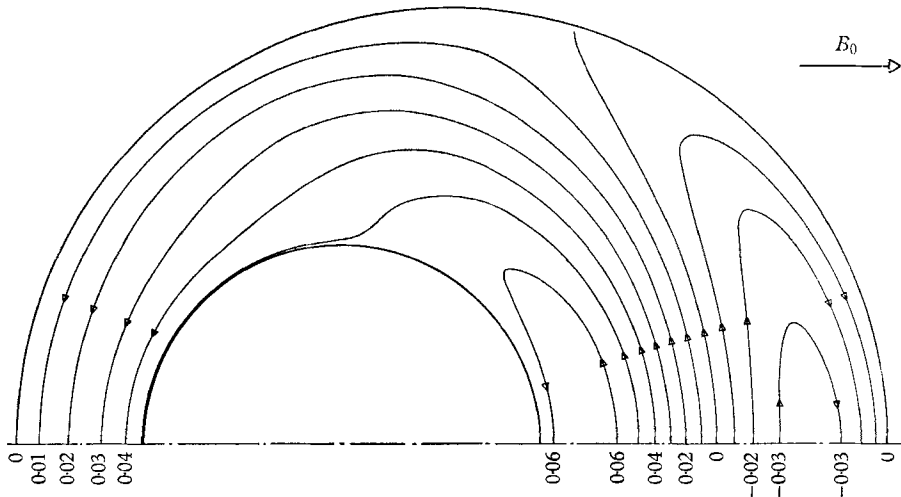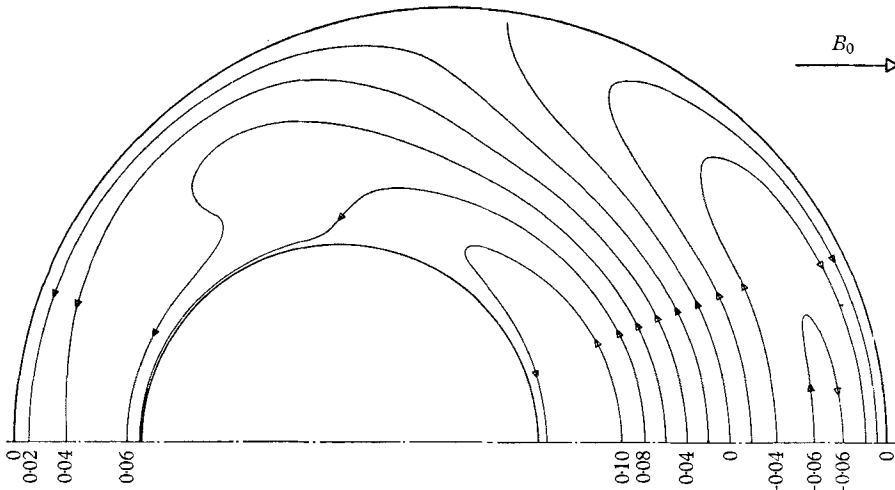

FIGURE 9. Distribution of induced magnetic field for eccentric cylinders at $M = 1$. Contours of $B_z \eta^{\frac{1}{2}}/\mu a^2 P \sigma^{\frac{1}{2}}$ at intervals of 0·01. Value on inner boundary is 0·0504.

FIGURE 10. Distribution of induced magnetic field for eccentric cylinders at $M = 5$. Contours of $B_z \eta^{\frac{1}{2}}/\mu a^2 P \sigma^{\frac{1}{2}}$ at intervals of 0·02. Value on inner boundary is 0·0826.

velocity in the wide gap decreases. Eventually a stage is reached when current can flow in the central part of the narrow gap in the general direction of the local induced e.m.f and, thereafter, the velocity in both gaps decreases with further increase in M.

The current line pattern for $M = 20$ is shown in figure 11. This pattern is similar in many respects to that for the concentric case at the same value of M, figure 5, but there is the important difference that there is a net current flowing right around the inner cylinder. This feature has been explained by Todd (1967).
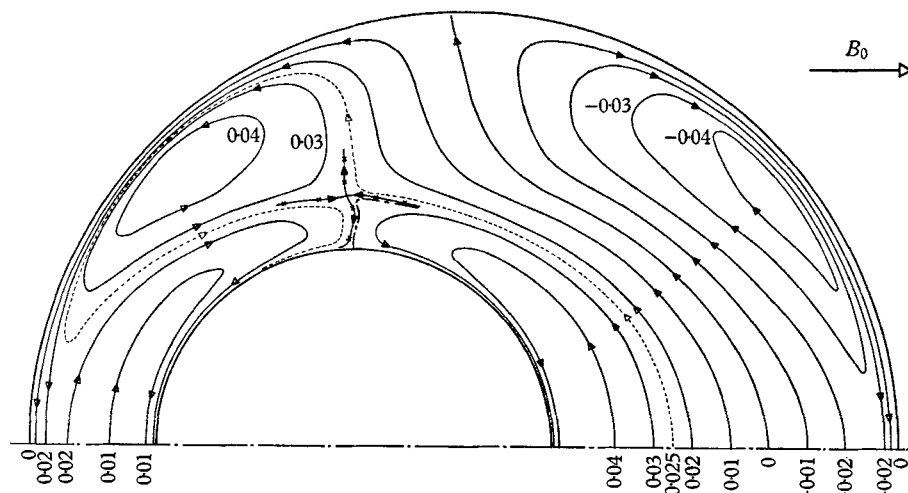

FIGURE 11. Distribution of induced magnetic field for eccentric cylinders at $M = 20$. Contours of $B_z \eta^{\frac{1}{2}}/\mu a^2 P \sigma^{\frac{1}{2}}$ at intervals of 0·01. Value on inner boundary is 0·0269. — × — × —, stagnation point current line, value 0·0267; — — — —, current line with same value as inner boundary.

The excess current flowing up the wider core returns *via* the boundary layers of the narrower side. Todd suggested that this excess current would split equally between each boundary layer, but figure 11 shows that this is not necessarily the case. All that is required is that the current in each boundary layer of the inner core should be equal for $M \gg 1$ and this can be achieved in a number of ways. In the case shown in figure 11 all of the current flowing up the narrow inner core returns via the boundary layer on the inner cylinder, this boundary-layer current being slightly augmented by some current from the wide inner core, whereas most of the excess current from the wide inner core returns down the boundary layer on the outer cylinder. The presence of the regions of pronounced maxima in $|B_z|$ in the vicinity of $\theta = \pm 45°$, $\pm 135°$ (already noted for the concentric case) gives rise to quite complicated current line patterns and some current flowing up the wider core loops almost right around the region of maximum $|B_z|$ before flowing down the boundary layer on the inner cylinder on the side of the narrower gap.

Saddle-points occur in the distribution of B_z at $M = 20$ for the eccentric cylinders of figure 11, in the vicinity of $\theta = \pm 90°$ near the inner cylinder and at $\theta = 0°, 180°$ near the outer cylinder. At the saddle-points a current line intersects itself and there is a stagnation point in the current flow. Part of the stagnation

point current line near $\theta = 90°$ is shown in figure 11. The value of B_z at the saddle points near $\theta = \pm 90°$ and at $\theta = 180°$ determine the way the excess current from the wide inner core divides between the boundary layers on the two cylinders. If B_{zi} denotes the value on the boundary of the inner cylinder and B_z (s90), B_z (s180) the values at the saddle-points near $\theta = 90°$ and at $\theta = 180°$
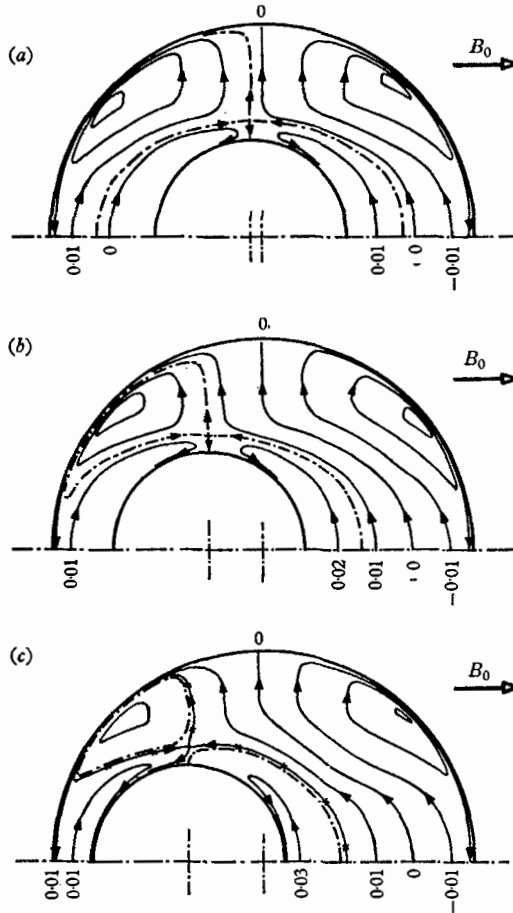

FIGURE 12. Current flow pattern at $M = 40$. Contours of $B_z \eta^{\frac{1}{2}}/\mu a^2 P \sigma^{\frac{1}{2}}$ at intervals of 0·01. (a) $\gamma/a = 0·1209$; — — — —, stagnation point current line, value 0·00298 is same as for inner boundary. (b) $\gamma/a = 0·5543$; — — — —, stagnation point current line, value 0·0137 is same as for inner boundary. (c) $\gamma/a = 0·7744$; — × — × —, stagnation point current line, value 0·0175; — — — —, current line with same value as inner boundary, 0·0191.

respectively, then the proportion of the excess core current which passes directly to the boundary layer of the inner cylinder is $(B_{zi} - B_z(s90)/B_{zi}$, and the remainder is forced out to the boundary layer of the outer cylinder by the presence of the maximum in $|B_z|$ near $\theta = \pm 135°$. Some of this current later leaves the boundary layer of the outer cylinder and crosses the gap to augment further the boundary-layer current on the inner cylinder. The proportion of the

excess core current which follows this path is $(B_z(s90) - B_z(s180))/B_{z_i}$. For the case shown in figure 11, $B_{z_i} = 0.0269$, $B_z(s90) = 0.0267$ and $B_z(s180) = 0.0218$, in non-dimensional terms, and $2/269$ of the excess core current passes directly to the inner cylinder boundary layer, $49/269$ is the additional amount which reaches the inner cylinder boundary layer after passing first to the outer cylinder boundary layer and $218/269$ is the proportion which remains in the outer cylinder boundary layer at $\theta = 180°$.

The current line patterns at $M = 40$ for three eccentricities are shown in figure 12. Comparison of the pattern at $M = 40$ for $\gamma/a = 0.5543$ (figure 12*b*) with that at $M = 20$ (figure 11) shows that, at the higher value of M, the 'wakes' have become less diffuse and that now $B_z(s90) = B_{z,i} = 0.0137$, so that the current line which branches at $\theta = \pm 90°$ has the same value of B_z as applies to the inner cylinder boundary. Hence, none of the excess current from the wide inner core can pass directly to the boundary layer of the inner cylinder and all of it is forced out first to the boundary layer of the outer cylinder. Since

$$B_z(s180) = 0.0128 < B_{z_i},$$

some of the excess core current eventually leaves the outer cylinder boundary layer to cross the gap between the cylinders and augment the boundary layer on the inner cylinder. This proportion, $9/128$, is approximately one-third of the proportion which followed a similar path at $M = 20$. In fact, it will follow from later discussion that, for this eccentricity, ultimately all of the excess core current remains in the boundary layer of the outer cylinder as M is increased indefinitely.

The three current flow patterns of figure 12 show how eccentricity affects the relative magnitudes of B_{z_i}, $B_z(s90)$ and $B_z(s180)$. The sequence of current flow patterns for $\gamma/a = 0.5543$ shows that ultimately $B_z(s90)$ becomes equal to B_{z_i} as M is increased indefinitely. The same development is observed in all the solutions calculated, the only effect on it of increasing eccentricity being to delay its completion to higher values of M. Whereas $B_z(s90) = B_{z_i}$ at $M = 40$ for all values of $\gamma/a \leqslant 0.5543$, this stage has not yet been reached at $M = 40$ for larger eccentricities. For example, at $M = 40$, $\gamma/a = 0.7744$, $B_z(s90) = 0.0175$ and $B_{z_i} = 0.0191$. However, there is no apparent reason why the observed trend of $B_z(s90) \to B_{z_i}$ as M increases will not continue until the two values are equal and it is considered that, for all eccentricities studied here, the ultimate current flow pattern for $M \gg 1$ will be similar to those for $\gamma/a \leqslant 0.5543$ in this respect, that all of the excess core current is forced out to the boundary layer of the outer cylinder. Whether all of this current remains in the outer cylinder boundary layer or whether some returns across the gap to the inner cylinder boundary layer depends on whether $B_z(s180) >$ or $< B_{z_i}$, and this, in turn, depends on the eccentricity, even when $M \gg 1$. It has been observed in an earlier section that, for $M \gg 1$, the currents in each boundary layer of the inner cores must be equal and the distribution of B_z in the cores is linear in x. If the thickness of the boundary layers is neglected these considerations lead to the result that $B_{z_i}/B_z(s180) = 2\gamma/(b-a)$ for $M \gg 1$. Hence, when $\gamma < \frac{1}{2}(b-a)$, $B_z(s180) > B_{z_i}$ and all the excess current from the wide inner core remains in the outer cylinder boundary layer but, when $\gamma > \frac{1}{2}(b-a)$, a proportion of the excess current, viz.

15

$(B_{z_i} - B_z(\text{s}180))/B_{z_i}$, ultimately reaches the boundary layer of the inner cylinder in the manner described above. The critical value of γ/a for the cylinders considered lies between 0·59 and 0·60. The points discussed are illustrated by the patterns of figure 12. For $\gamma/a = 0·1209$, $B_{z_i} = 0·00298$, $B_z(\text{s}180) = 0·01250$ at
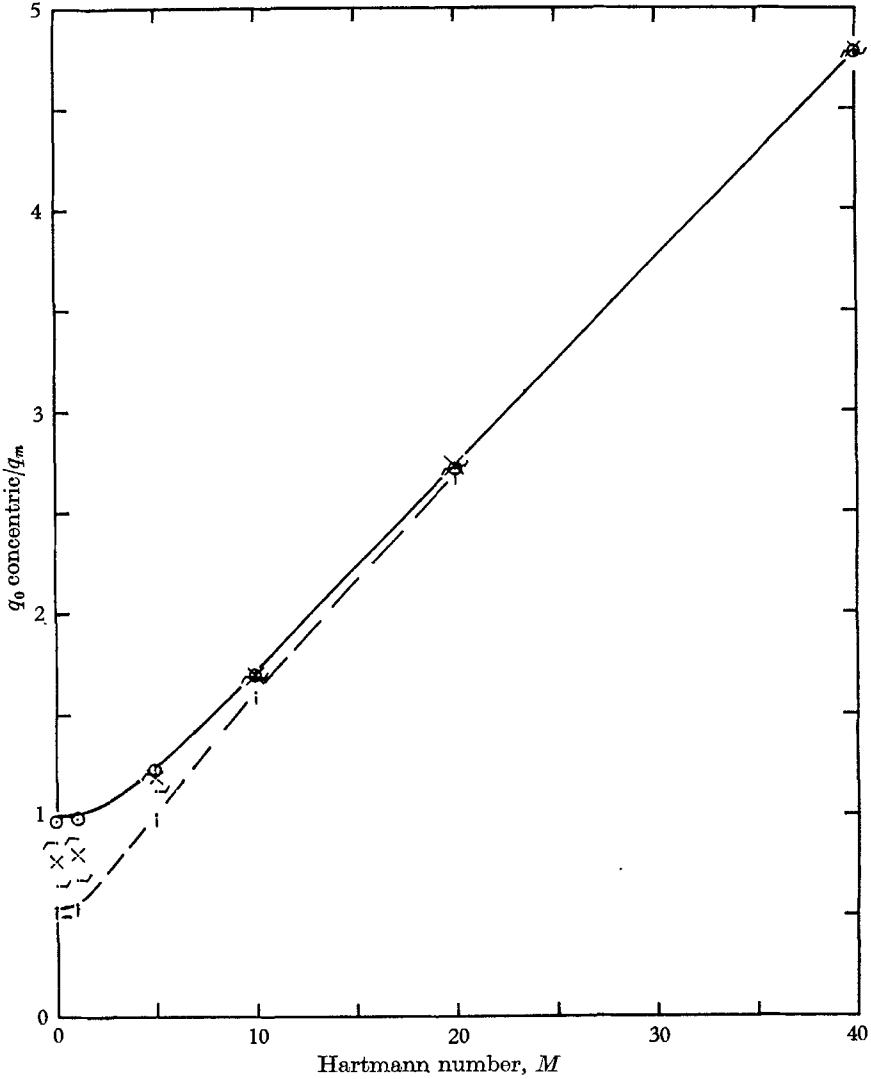

FIGURE 13. Flow rates for concentric and eccentric cylinders. q_0 denotes Poiseuille flow rate and q_M denotes Hartmann flow rate. ——, concentric cylinders; ⊙, $\cap$, ×, $\cup$, i, $\gamma/a = 0·1209$, 0·3867, 0·5543, 0·7744 and 1·0000, respectively.

$M = 40$. The case of $\gamma/a = 0·5543$, which has been discussed above, is so close to the critical that the final pattern in which all the excess core current remains in the outer cylinder boundary layer is reached only for M in excess of 40. For $\gamma/a = 0·7744$, $B_{z_i} = 0·0191$, $B_z(\text{s}180) = 0·0124$.

The dependence of flow rate on M is shown for the concentric case and the

eccentric cases studied in figure 13. The flow rate is plotted as the ratio of the Poiseuille flow for concentric cylinders to the actual flow for the given geometry at the same pressure gradient. At $M = 0$, corresponding to Poiseuille flow, figure 13 illustrates the well known result that eccentricity of the inner cylinder gives an increased flow rate for a given pressure gradient. However, the effect
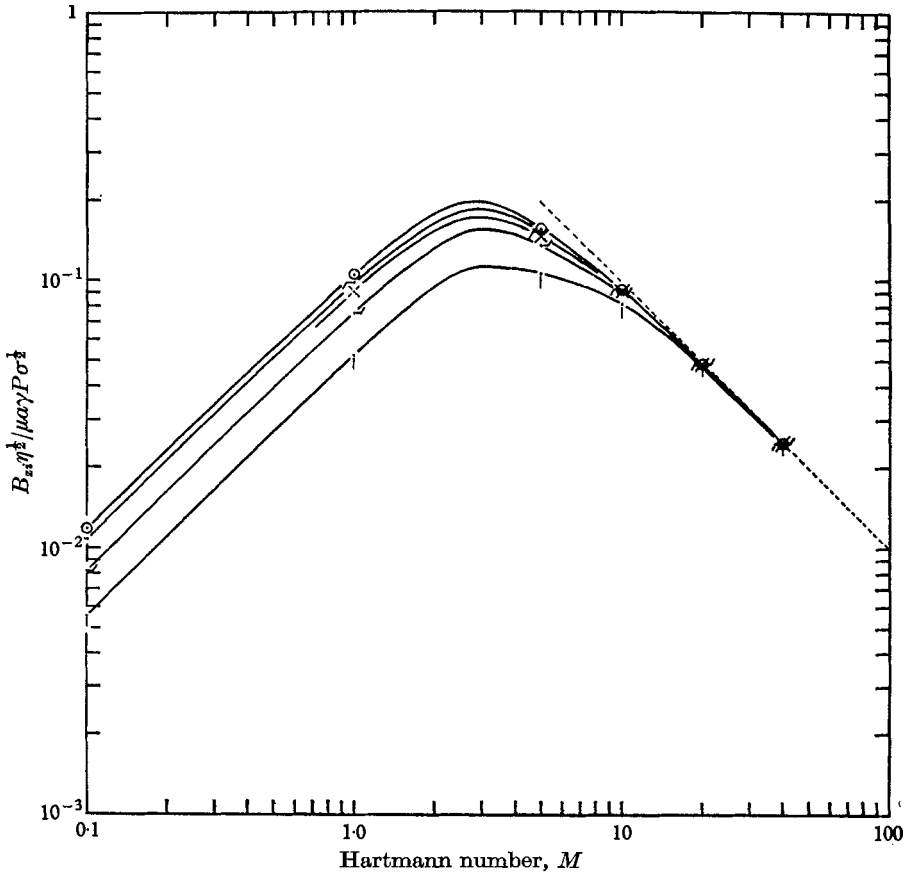

FIGURE 14. Current flowing around annulus per unit length. $\odot$, $\nearrow$, $\times$, $\swarrow$, i, numerical solutions for $\gamma/a = 0.1209$, 0.3867, 0.5543, 0.7744 and 1.0000, respectively; ————, result from large Hartmann number analysis.

of an applied transverse magnetic field is both to reduce the flow rate and also to reduce the effect of eccentricity on flow rate, and for $M \geqslant 20$ all geometries give very nearly the same flow rate as the concentric case at the same pressure gradient. At $M = 20$, the flow rate for the maximum eccentricity studied is only 1.7 per cent greater than that for the concentric case. All curves of figure 13 become asymptotic to the one straight line, and for $M > 20$ the flow rate has become inversely proportional to M within a very good accuracy. The constant of proportionality depends only on the ratio b/a. From figure 13 the slope of the straight line asymptote is 0.1027 as compared to the value 0.1039 calculated from Todd's result for $M \gg 1$.

The dependence of the value of B_{z_i} on the boundary of the inner cylinder on eccentricity and on Hartmann number is shown in figure 14, B_{z_i} being combined with the eccentricity, γ, in the dimensionless quantity $B_{z_i}\eta^{\frac{1}{2}}/\mu a\gamma P\sigma^{\frac{1}{2}}$. As pointed out in an earlier section, B_{z_i}/μ equals the net amount of current flowing around the annulus per unit length. At low Hartmann numbers the curves for the different eccentricities are different but they all appear to be asymptotic as $M \to 0$ to a line of unit slope on the log-log plot, indicating that, for $M \ll 1$, the current looping the annulus is proportional to M, the constant of proportionality being a function of the eccentricity. For each geometry the maximum current looping the annulus is generated at a Hartmann number very close to 3.† For larger values of M, the curves for the different eccentricities collapse together and become asymptotic to a line of slope, -1, corresponding to the relationship,

$$B_{z_i} = \mu P\gamma B_0^{-1}, \tag{23}$$

which applies for all eccentricities and is the same as the result obtained by Todd (1967) for $M \gg 1$. At $M = 20$, the results for all cases fall in a range of 1·8% and the result for the maximum eccentricity has approached to within 4·7% of the value given by the asymptotic expression (23).

5. Some details of accuracy of computations

The excellent agreement between the numerical solutions for the larger values of M and the results of Todd's solution for $M \gg 1$ is strong evidence for the accuracy of the numerical solutions. A number of tests of the accuracy of the numerical solutions was carried out during computation as described in §3. Some results of these are summarized here.

When the values of V and B obtained from the numerical solution on the finest mesh were inserted into (6) and (7) the maximum residuals were found to be between 10^{-6} and 10^{-5} times the order of magnitude of V and B. For coarser mesh lengths the residuals were found to vary approximately as h^4.

The integral checks on the overall force balance, described in §3, gave agreement within 0·05% for $M \leqslant 5$, 0·5% at $M = 10$, 1% at $M = 20$ and 2% at $M = 40$. The check on B_{z_i} gave essentially similar results. The calculation of both integral checks involves quantities which are the small differences between much larger quantities and this feature becomes more pronounced at larger Hartmann numbers, probably giving rise to an over-estimate of errors in the integral checks.

6. Conclusion

The numerical solutions of Hartmann flows at low to moderate Hartmann numbers show how the patterns of velocity and of current flow in annular channels develop as M increases. The details of the development of current flow

---

† It would be interesting to locate the maxima more precisely, in view of the result (Todd 1966), for the simple case of Hartmann flow between parallel planes, that the maximum power is developed from such a magnetohydrodynamic generator at $M = 3\cdot0$.

pattern for eccentric cylinders are particularly interesting and the effects of varying eccentricity on all significant features of the patterns have been determined.

For the geometries studied the solutions begin to display the essential features of the high Hartmann number flow at Hartmann numbers between 10 and 20, and at $M = 40$ the numerical solutions for channels with eccentricities $0 \leqslant \gamma/a \leqslant 0.5543$ are virtually indistinguishable from the results of the high Hartmann number analysis except that the 'wakes' are still relatively diffuse. For larger eccentricities such close agreement with the high Hartmann number analysis would be reached only for $M > 40$.

The numerical method developed for solution of Hartmann flows has proved to be efficient at Hartmann numbers in the range $0.1 \leqslant M \leqslant 40$ and the excellent agreement between the results of the numerical solution at large values of M and the results of the high Hartmann number analysis gives solid ground for confidence in the application of the numerical method to problems for which there are, as yet, no analytical solutions available.

REFERENCES

GOLD, R. 1962 *J. Fluid Mech.* **13**, 505.

HASIMOTO, H. 1960 *J. Fluid Mech.* **8**, 61.

RICHARDSON, L. F. & GAUNT, J. A. 1926 *Phil. Trans.* A **226**, 299.

RUSSELL, D. B. 1962 *Aero. Res. Counc. R. & M.* no. 3331.

SHERCLIFF, J. A. 1953 *Proc. Camb. Phil. Soc.* **49**, 136.

SHERCLIFF, J. A. 1956 *J. Fluid Mech.* **1**, 644.

THOM, A. & APELT, C. J. 1961 *Field Computations in Engineering and Physics.* New York: Van Nostrand.

TODD, L. 1966 *Phys. Fluids* **9**, 1602.

TODD, L. 1967 *J. Fluid Mech.* **28**, 371.

UFLYAND, Y. S. 1961 *Sov. Phys. Tech. Phys.* **5**, 1194.

WAECHTER, R. T. 1968 *Proc. Camb. Phil. Soc.* **64**, 1165.

YOUNG, D. 1954 *Trans. Am. Math. Soc.* **76**, 92.